

Analysis and Implementation of a Tubular Motor with Halbach Magnet Array

W.-J. Kim, M. T. Berhan, D. L. Trumper and J. H. Lang
Massachusetts Institute of Technology, 77 Massachusetts Avenue, Cambridge, MA 02139

Abstract—In the machine tool industry, direct-drive linear motor technology is of increasing interest as a means to achieve high acceleration, and to increase reliability. This paper discusses the analysis, design and operating characteristics of a novel ironless tubular linear motor that incorporates a magnet array with a magnetization pattern inspired by the Halbach array used in synchrotron light sources. The advantages of such a motor are that it is free of cogging, has efficient cooling, and has low inductance. We derive magnetic field solutions, force relations and commutation laws for the motor. Test results such as thrust measurements and step response are also given to confirm the analysis.

I. INTRODUCTION

Our work is motivated by the desire to develop a direct-drive linear actuator for machine tool applications. The applications for such a motor range from material handling devices to semiconductor wafer stepping applications, diamond turning machines and other precision applications. This tubular motor is intended to demonstrate the utility for such a drive unit in mid- to high-thrust applications. Many commercial linear synchronous motors use unipolar or linear brushless DC type actuators with a linear encoder. The references [1]–[2] are examples of tubular linear synchronous motors. Tubular linear induction motors in various applications can be found in the literature, such as [3]. A tubular linear permanent-magnet synchronous motor was chosen for our study in light of its advantages: 1) higher maximum speeds and acceleration limits, 2) minimization of power loss due to end-turn effects, 3) higher position accuracy without anti-backlash devices, 4) no direct physical constraint in the axial direction of propulsion, 5) no power loss in rotary-linear power conversion, 6) no friction except in the ball bearings that support the platen weight.

The platen (slider) of the motor employs a tubular version of the Halbach magnet array [4]. An ironless Halbach magnet array made up of square blocks has $\sqrt{2}$ times stronger field than conventional magnet arrays with the same magnet volume and has no third-order harmonics on its strong side [5]. Even non-square Halbach arrays

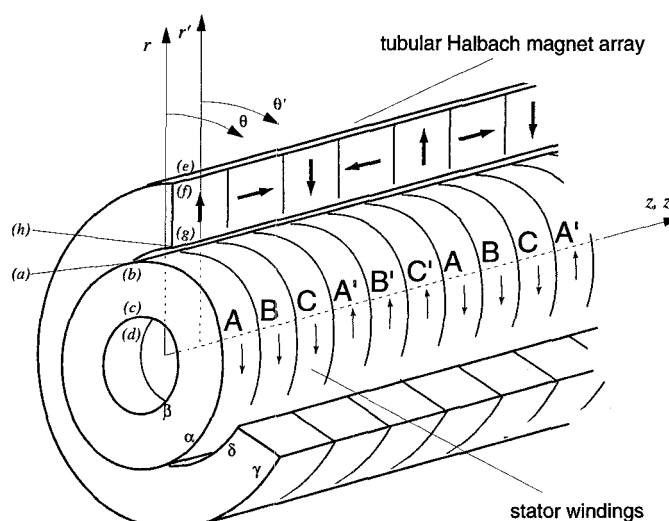


Fig. 1. Tubular Motor Model

produce higher force than conventional arrays when there is no magnet back-iron as in our design [6].

In the following section, a continuum model and magnetic field solutions for the class of tubular linear permanent-magnet motors are given. The results are summarized in the main text, with details presented in the Appendix. The motor fields are derived analytically in terms of Bessel functions. The motor force is evaluated with the Maxwell stress tensor using the field solutions in the tubular geometry. It is cumbersome to invert the field solutions. We therefore derive commutation laws for the motor by approximating the tubular motor as a planar motor. We next present the mechanical and thermal design of the tubular motor, followed by the control and instrumentation of the system. Finally, we provide preliminary thrust measurements and step response to confirm the analyses.

II. TUBULAR MOTOR ANALYSIS

A. Tubular Motor Model

Fig. 1 is a model for a three-phase tubular linear motor with a Halbach magnet array. Letters (a)–(h) represent the surfaces at the indicated boundaries and Greek letters α – δ denote the inner and outer radii of the magnets and

the stator. A base coordinate frame is attached to the stator. The magnet array carries a primed coordinate frame which is displaced from the base coordinate frame by a vector $z_0 \mathbf{i}_z$. Thus z_0 is the lateral displacement of the magnet array relative to the stator. The magnetization of the magnet array is represented as

$$\mathbf{M} = \sum_{n=-\infty}^{\infty} \left[\frac{\tilde{M}_{rn}}{r'} e^{-jk_n z'} \mathbf{i}_{r'} + \tilde{M}_{zn} e^{-jk_n z'} \mathbf{i}_{z'} \right], \quad (1)$$

where the pitch of the motor is l , and the spatial wavenumber of the n th harmonic is $k_n = 2\pi n/l$. We further define $\gamma_n = |k_n|$. Here \tilde{M}_{rn} and \tilde{M}_{zn} are the complex Fourier coefficients of n th-order radial and axial magnetization components, respectively. Similarly, we can represent the current density in a Fourier series. The exact solution with a current distribution uniform in radius contains integrals of Bessel functions that cause a significant analytical burden. In this paper, we instead adopt a current distribution proportional to the inverse of the radius, as the Poisson equation has solutions in a simpler form for this distribution. This approximate solution gives a good approximation to the exact result if the radius of the current carrying tube is sufficiently large relative to the thickness of the windings. Specifically, we assume that the free current density in the stator has the distribution

$$\mathbf{J}_f = \sum_{n=-\infty}^{\infty} \frac{\tilde{J}_{\theta n}}{r} e^{-jk_n z} \mathbf{i}_{\theta}, \quad (2)$$

See [7] for the expressions of \tilde{M}_{rn} and \tilde{M}_{zn} of the Halbach magnet array and $\tilde{J}_{\theta n}$ of the surface-wound stator current. Fourier series representations are also applied to the magnetic flux density \mathbf{B} and the magnetic field intensity \mathbf{H} .

B. Poisson Equation for Vector Potential

As in [5], the vector Poisson equation for the vector potential \mathbf{A} can be derived as

$$\nabla^2 \mathbf{A} = -\mu_0 (\mathbf{J}_f + \nabla \times \mathbf{M}). \quad (3)$$

In the context of permanent-magnet machines, \mathbf{J}_f represents the stator current. We can think of the term $\nabla \times \mathbf{M}$ as an equivalent current sources which represents the permanent magnets.

In an axisymmetric two-dimensional application where the magnetic fields lie in the zr -plane with no dependence on θ , the vector potential is purely θ -directed with r - and z -dependences only. In this case, the Fourier coefficients $\tilde{A}_{\theta n}$ of the θ -component of the vector potential satisfy the following scalar Poisson equations in the magnet and the current regions, respectively.

$$\frac{d^2 \tilde{A}_{\theta n}}{dr'^2} + \frac{1}{r'} \frac{d\tilde{A}_{\theta n}}{dr'} - \left(k_n^2 + \frac{1}{r'^2} \right) \tilde{A}_{\theta n} = \mu_0 \frac{jk_n}{r'} \tilde{M}_{rn} \quad (4)$$

$$\frac{d^2 \tilde{A}_{\theta n}}{dr^2} + \frac{1}{r} \frac{d\tilde{A}_{\theta n}}{dr} - \left(k_n^2 + \frac{1}{r^2} \right) \tilde{A}_{\theta n} = -\mu_0 \frac{1}{r} \tilde{J}_{\theta n} \quad (5)$$

A particular solutions to the above Poisson equations for non-zero n are $\tilde{A}_{\theta np} = -\frac{j\mu_0}{k_n r'} \tilde{M}_{rn}$ and $\frac{\mu_0}{k_n^2 r} \tilde{J}_{\theta n}$, respectively.

C. Field Solutions

In order to analyze the tubular motor, we apply the continuum electromechanical approach developed by Melcher [8]. We derived the field solution, force and electrical terminal relation for linear permanent-magnet levitators in a previous paper [5]. In the present paper, we present the analysis for tubular motors in axisymmetric cylindrical geometry. As derived in the Appendix, the transfer relations which relate the fields evaluated at the surfaces identified in the model of Fig. 1 are

$$\tilde{B}_{zn}^e = -\gamma_n \frac{K_0(\gamma_n \gamma)}{K_1(\gamma_n \gamma)} \tilde{A}_{\theta n}^e \quad (6)$$

$$\begin{bmatrix} \tilde{B}_{zn}^f \\ \tilde{B}_{zn}^g \end{bmatrix} = -k_n^2 \begin{bmatrix} F_0(\delta, \gamma) & G_0(\gamma, \delta) \\ G_0(\delta, \gamma) & F_0(\gamma, \delta) \end{bmatrix} \begin{bmatrix} \tilde{A}_{\theta n}^f \\ \tilde{A}_{\theta n}^g \end{bmatrix} - j\mu_0 k_n \tilde{M}_{rn} \begin{bmatrix} F_0(\delta, \gamma)/\gamma + G_0(\gamma, \delta)/\delta \\ G_0(\delta, \gamma)/\gamma + F_0(\gamma, \delta)/\delta \end{bmatrix} \quad (7)$$

$$\begin{bmatrix} \tilde{B}_{zn}^h \\ \tilde{B}_{zn}^a \end{bmatrix} = -k_n^2 \begin{bmatrix} F_0(\alpha, \delta) & G_0(\delta, \alpha) \\ G_0(\alpha, \delta) & F_0(\delta, \alpha) \end{bmatrix} \begin{bmatrix} \tilde{A}_{\theta n}^h \\ \tilde{A}_{\theta n}^a \end{bmatrix} \quad (8)$$

$$\begin{bmatrix} \tilde{B}_{zn}^b \\ \tilde{B}_{zn}^c \end{bmatrix} = -k_n^2 \begin{bmatrix} F_0(\beta, \alpha) & G_0(\alpha, \beta) \\ G_0(\beta, \alpha) & F_0(\alpha, \beta) \end{bmatrix} \begin{bmatrix} \tilde{A}_{\theta n}^b \\ \tilde{A}_{\theta n}^c \end{bmatrix} + \mu_0 \tilde{J}_{\theta n} \begin{bmatrix} F_0(\beta, \alpha)/\alpha + G_0(\alpha, \beta)/\beta \\ G_0(\beta, \alpha)/\alpha + F_0(\alpha, \beta)/\beta \end{bmatrix} \quad (9)$$

$$\tilde{B}_{zn}^d = \gamma_n \frac{I_0(\gamma_n \beta)}{I_1(\gamma_n \beta)} \tilde{A}_{\theta n}^d. \quad (10)$$

The geometric parameters $F_0(\cdot, \cdot)$ and $G_0(\cdot, \cdot)$ are [8]

$$F_0(x, y) = -\frac{I_1(k_n x) K_0(k_n y) + K_1(k_n x) I_0(k_n y)}{k_n \{I_1(k_n y) K_1(k_n x) - K_1(k_n y) I_1(k_n x)\}} \quad (11)$$

and

$$G_0(x, y) = -\frac{1}{k_n^2 x \{I_1(k_n y) K_1(k_n x) - K_1(k_n y) I_1(k_n x)\}}, \quad (12)$$

where $I_\nu(\cdot)$ and $K_\nu(\cdot)$ are modified Bessel functions.

The terms containing \tilde{M}_{rn} and $\tilde{J}_{\theta n}$ represent sources in the magnet and current regions, respectively. The other source term \tilde{M}_{zn} enters through boundary conditions and does not appear in the transfer relations. Since (8) describes the transfer relations in the air gap, it has no source term. Equations (6) and (10) account for the regions outside the boundary (e) and inside the boundary (d), respectively.

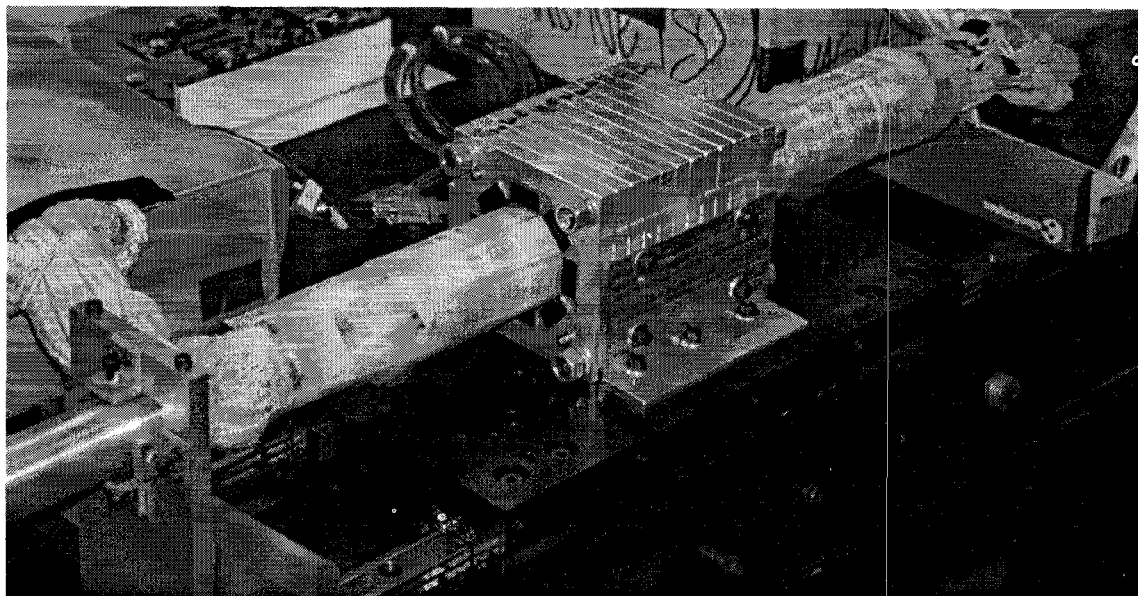


Fig. 2. Test Rig

These transfer relations express the constraints on field and potential quantities imposed by the magneto-quasistatic form of Maxwell's equations. In our case, the transfer relations give eight equations in sixteen unknowns. The additional eight required independent equations for a unique field solution come from the continuity conditions on field and potential at each of the four boundaries. Using these conditions along with the transfer relations, we can solve for the magnetic field throughout the region. A more detailed derivation for these solutions is in the Appendix.

III. DESIGN OF A PERMANENT-MAGNET TUBULAR LINEAR MOTOR

We discuss mechanical and thermal design issues of the tubular motor in this section.

A. Mechanical Design

We have designed a three-phase, 52.32-mm pitch motor with 300-mm axial travel. Fig. 2 gives a picture of the system. This motor is sized via our analyses to produce 125 N at a peak current density of 3×10^6 A/m², with a power dissipation of 97 W over the 9-pitch length (471 mm) which supports the windings. The three pitches of four magnet orientation directions apiece are made from twelve aluminum plates, each holding eight NdFeB magnets arranged in an octagonal ring, circumscribing a circle 67.44 mm in diameter as shown in Fig. 3. The rectangular magnets are characterized by a remanence $B_r = 1.08$ T, and are 12.7 mm \times 12.7 mm \times 25.4 mm in size. The Halbach array consists of three pitches with four octagonal

rings per pitch. So there are a total of 96 such rectangular magnets on the platen.

This compact tubular configuration of the motor is designed to address limitations of planar permanent-magnet motor designs. When the entire stator circumference is surrounded by the magnet array, end turns are eliminated, thereby increasing the motor efficiency. This configuration also avoids edge effects because the magnet ring sees a continuous stator circumference. The cross-section of the magnet ring is an octagon rather than a circle because a radially magnetized ring magnet of the proper dimensions was difficult to obtain (Fig. 3). The air gap between the magnets and the windings is 2.54 mm at the closest point; this was chosen to make it easy to build and align the stator in this first prototype. The plates are located in position by long rods which extend through each

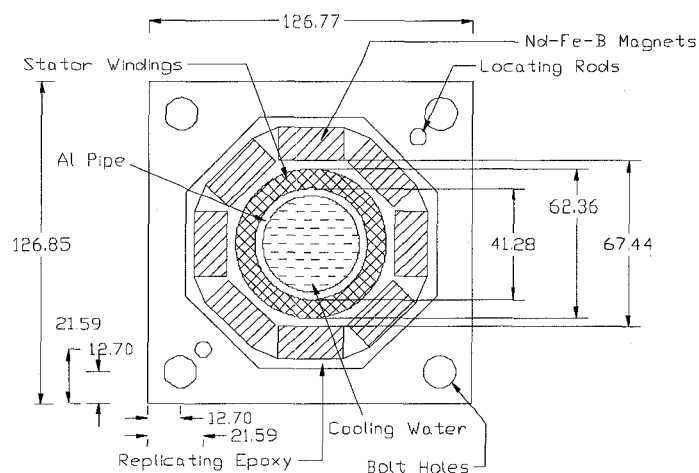


Fig. 3. Magnet Chassis

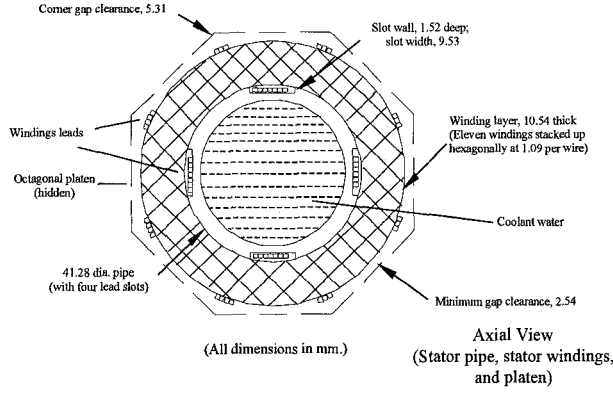


Fig. 4. Winding Leads

plate at the corners. The plate assembly is mounted to a steel carriage platen (total mass: 31 kg) riding atop four precision ball-bearing linear guides. The guide rails are set into a precision ground cast iron bed. The magnet chassis together with the carriage plate form the moving platen.

The stator uses 3 phases over 9 pitches. The motor's fifty-four individual coils (six coils per pitch) are wound from 76 turns of AWG #14 copper wire. Each coil is wound on the outside of an aluminum pipe and the coils have an outer diameter of 62.36 mm. The start leads of each coil are run under the windings through one of four slots running axially along the stator pipe. The finish leads of each coil are run over the windings through the corner gaps between the magnets and the stator surface. The wire ends are then connected in series for each phase, leading to their respective amplifiers and power supplies. This lead arrangement may be seen in Fig. 4.

B. Thermal Design

One of the reasons for us to use a moving-magnet-stationary-winding scheme is to make cooling easy. The windings are directly wound on the aluminum pipe, through which coolant flows. The outer and inner diameters of the pipe are 41.28 mm and 34.75 mm. The system is sized at a nominal flow rate of up to 0.5 kg/s.

In order to develop a thermal model of the stator, a few assumptions are made. 1) All heat energy generated in the windings is transferred through the stator tube wall into the coolant fluid. 2) The thermal path from the stator windings to the coolant does not include the extra length of the stator pipe past the coils. 3) The windings' outer surface is modeled as a perfect insulator.

1) *Surface Temperature Calculations:* We define T_1 , T_2 and T_3 as the temperatures at the inner surface of the aluminum pipe, at the inner surface of the winding (at $r = \beta$) and at the outer surface of the winding (at $r = \alpha$), respectively. From Newton's law of cooling, T_1 is calculated as

$$T_1 = \frac{q_v}{hA_s} + T_M, \quad (13)$$

where q_v is the heat generation density in the windings, h is the heat transfer convection coefficient, A_s is the internal surface area under the stator winding, and T_M is the coolant bulk temperature [9]. Since the thermal conductivity of aluminum is large, T_2 was assumed to be equal to T_1 . T_3 was calculated in the following way. We assume that q_v is constant throughout the stator. We take $q_v = P_v PF$, where P_v is the power dissipation density in the copper. The packing factor $PF = 0.67$ represents the volumetric percent copper in our windings. For a heat-generating cylindrical volume the temperature distribution is given [9] by

$$T(r) = \frac{-q_v}{4k} r^2 + \frac{q_v}{2k} \alpha^2 \ln r + \left[\frac{q_v}{4k} \beta^2 - \frac{q_v}{2k} \alpha^2 \ln \beta + T_2 \right]. \quad (14)$$

where k is the thermal conductivity of the winding region. This relation holds in the region between $r = \alpha$ and $r = \beta$.

2) *Experimental Determination of Windings' Transverse Thermal Conductivity:* We want to determine the value of the thermal conductivity of the stator. The hexagonal packing of the magnet wires will give much less thermal conductivity than for pure copper. Rearranging (14) gives the windings' transverse thermal conductivity.

$$k = \frac{q_v}{T_3 - T_2} \left[\frac{\beta^2 - \alpha^2}{4} + \frac{\ln \alpha + \ln \beta}{2} \alpha^2 \right] \quad (15)$$

We assume the thermal conductivity throughout the stator winding region is uniform. Measuring the temperatures T_2 and T_3 directly, we calculated an average value of $k = 0.15$ W/m-K. This value is three orders of magnitude smaller than the value of pure copper at 398 W/m-K, but is five times greater than the thermal conductivity of air at room temperature, 0.03 W/m-K. This is understandable since the windings have one-third air by volume. Also each wire's epoxy-bonding coats are the only solids that touch and nominally make line contact.

3) *Thermal Limits:* The thermal limit of our motor is dominated by the low thermal conductivity k of the stator windings. This limit is about 3.0×10^6 A/m², for a thrust load of 125 N with a surface temperature $T_3 = 73^\circ\text{C}$. With higher current loads, T_3 passes 80°C , a temperature at which the NdFeB magnets may begin to lose strength. At $J = 4 \times 10^6$ A/m² and $f_z = 167$ N, $T_3 = 113^\circ\text{C}$. At this point the thermoset temperature of the windings' bonding layer, approximately 110 – 120°C , becomes a limiting factor. All these temperatures are at steady-state operations.

Square magnet wire would have a higher packing factor by 10–20%, if properly wound. This would allow for lower heat generation and current density for a given thrust, and should provide a higher overall thermal conductivity with less air present. One possible future solution for round and square wire coils may be to have them wound and encapsulated in a high thermal conductivity varnish or

epoxy which would take up the space between the wires and provide a better thermal path.

4) *Heat Generation Rate*: The model used for the current density in this paper does not account for the discontinuous nature of the coils. The packing factor PF is divided into the target winding region current density to get a higher density in the copper itself. We derive the overall heating by using the scaled current density and the actual copper volume. The heat generation density from the peak sinusoidal current distribution in the copper is then

$$P_v = \frac{(J/PF)^2}{2\sigma}, \quad (16)$$

where σ is the conductivity of copper (5.7×10^7 S/m). For a target winding region current density $J = 3 \times 10^6$ A/m², $P_v = 1.8 \times 10^5$ W/m³. The overall heat generation rate in the winding volume would then be 97 W in steady state.

IV. ELECTRICAL SYSTEM

A. Force

We can derive the force output of the tubular motor with the magnetic field solutions via the Maxwell stress tensor. As presented in [8], the stress tensor T_{ij} for magnetically linear materials associated with the Korteweg-Helmholtz force density is

$$T_{ij} = \mu H_i H_j - \delta_{ij} \frac{\mu}{2} H_k H_k. \quad (17)$$

We can evaluate the predicted force with the analytical Fourier series field solutions derived earlier. The transfer relations given in Section III.C and field solutions in tubular geometry are algebraically complicated. If the radii of the magnet and current regions are large compared with their thicknesses, we can use the force equations for planar linear motors given in [5]. Thus, to give an analytical result, we derive the commutation laws with the force equations in Cartesian coordinates. Here, the radial force component cancels due to the symmetry of the tubular motor. The axial thrust can be written [5] as

$$f_z = \mu_0 M_0 \eta_0 G N_m e^{-\gamma_1(\delta-\alpha)} \begin{bmatrix} \cos \gamma_1 z_0 & \sin \gamma_1 z_0 \end{bmatrix} \begin{bmatrix} i_a \\ i_b \end{bmatrix}, \quad (18)$$

where $\mu_0 M_0$ is the remanence of the permanent magnets, η_0 is the turn density of the winding in turns/m², and N_m is the number of magnet pitches in the stator. The constant G depends on the motor geometry and is defined as follows.

$$G = \frac{\sqrt{2} w l^2}{\pi^2} \left(1 - e^{-\gamma_1(\alpha-\beta)}\right) \left(1 - e^{-\gamma_1(\gamma-\delta)}\right), \quad (19)$$

where w is the average circumference of the air gap. The z_0 dependence has been explicitly retained since this variable represents the motion of the magnet array relative to the stator.

B. Commutation

Although the analysis can be carried out more generally, in the following we assume that the stator currents are sinusoidally distributed with a fundamental period of l and thus that \tilde{J}_n is equal to zero for $n \neq \pm 1$. Specifically, we let $\tilde{J}_1 = J_a + jJ_b$, and $\tilde{J}_{-1} = J_a - jJ_b$. The above assumption is reasonable since it is primarily the fundamental field components that are responsible for force production [7]. We propose to compensate the ripple force due to the higher-order harmonics via error mapping.

Under this assumption, the stator current density as a function of z simplifies to

$$\begin{aligned} J(z) &= \sum_{n=-\infty}^{\infty} \tilde{J}_n e^{-jk_n z} \\ &\cong (J_a + jJ_b) e^{-jk_1 z} + (J_a - jJ_b) e^{-jk_{-1} z} \\ &= 2J_a \cos \gamma_1 z + 2J_b \sin \gamma_1 z. \end{aligned} \quad (20)$$

The centers of the physical phase current densities J_A , J_B , J_C , J'_A , J'_B , J'_C are located on the stator at $z = 0$, $l/6$, $l/3$, $l/2$, $2l/3$, $5l/6$, and so forth. In other words,

$$\begin{aligned} J_A &= J(z = ml) = -J'_A \\ J_B &= J(z = ml + l/6) = -J'_B \\ J_C &= J(z = ml + l/3) = -J'_C, \end{aligned} \quad (21)$$

where m is an integer. Then, the following transformation holds between $[J_a \ J_b]^T$ and $[J_A \ J_B \ J_C]^T$.

$$\begin{bmatrix} J_A \\ J_B \\ J_C \end{bmatrix} = \begin{bmatrix} 2 & 0 \\ 2 \cos \frac{\pi}{3} & 2 \sin \frac{\pi}{3} \\ 2 \cos \frac{2\pi}{3} & 2 \sin \frac{2\pi}{3} \end{bmatrix} \begin{bmatrix} J_a \\ J_b \end{bmatrix} = T_{32} \begin{bmatrix} J_a \\ J_b \end{bmatrix} \quad (22)$$

The three-phase-to-two-phase transformation, T_{32} is given as

$$T_{32} = \begin{bmatrix} 2 & 0 \\ 1 & \sqrt{3} \\ -1 & \sqrt{3} \end{bmatrix}. \quad (23)$$

Then, the commutation law for the physical three-phase current $[i_A \ i_B \ i_C]^T$ with the desired thrust f_{zd} becomes

$$\begin{bmatrix} i_A \\ i_B \\ i_C \end{bmatrix} = \frac{e^{\gamma_1(\delta-\alpha)}}{\mu_0 M_0 \eta_0 G N_m} T_{32} \begin{bmatrix} \cos \gamma_1 z_0 \\ \sin \gamma_1 z_0 \end{bmatrix} f_{zd}. \quad (24)$$

This relation is used for the computed commutation of the motor in our test setup.

C. Control

For the purpose of control, we model the platen that carries magnet array as a pure mass. This does not account for any friction from the linear guide bearings, and assumes that there is no viscous friction in the bearings. It also assumes there is no detectable compliance in the

system's force loop from the base table through stator and the magnet chassis.

With a platen mass $M = 31$ kg, the transfer function from the displacement to force in continuous time is

$$G_p(s) = \frac{1}{Ms^2}. \quad (25)$$

The zero-order hold equivalent [10] of the plant is

$$\begin{aligned} G_p(z) &= (1 - z^{-1}) \mathcal{Z}\left(\frac{G_p(s)}{s}\right) \\ &= \frac{T_s}{2M} \frac{(z + 1)}{(z - 1)^2}, \end{aligned} \quad (26)$$

where the sampling time $T_s = 3.1$ ms is set at 20 times higher than the crossover frequency, $\omega_c = 100$ rad/s.

We implemented a lead-lag compensator for the tubular motor of the form

$$G_c(z) = 992480 \left(\frac{z - 0.99007}{z - 1} \right) \left(\frac{z - 0.90065}{z - 0.00654} \right). \quad (27)$$

The zero and the pole are separated by one decade to yield a phase margin of 55° .

D. Instrumentation

The tubular motor is controlled by a 90-MHz P54 Pentium-based personal computer. Position feedback is from a Sony Magnescale linear magnetic encoder with position resolution of $0.64 \mu\text{m}$ ($25 \mu\text{in}$), which is mounted to the side of the carrier platen. The motor commutation is computed on the basis of the measured motor position. The three resulting current commands are output through a 12-bit D/A board and sent to 3 voltage-to-current amplifiers which drive the coil windings. The motor temperature is measured by thermocouples through a 12-bit A/D board.

V. TEST RESULTS

In this section, we present preliminary test results, such as thrust measurements and step response of the tubular motor to confirm the analyses.

A. Thrust Measurements

The force output per peak ampere of our three-phase motor is calculated to be 34.4 N/A , and is taken as a constant value. Our experimental results show an average output of 26.9 N/A . For example, a 6.04-A peak phase current for a maximum current density in the winding region of $5 \times 10^6 \text{ A/m}^2$ produces a measured thrust value of 168 N . Our results return an average experimental power to force ratio of $1.02 \times 10^{-2} \text{ W/N}^2$. The expected value is $6.22 \times 10^{-3} \text{ W/N}^2$.

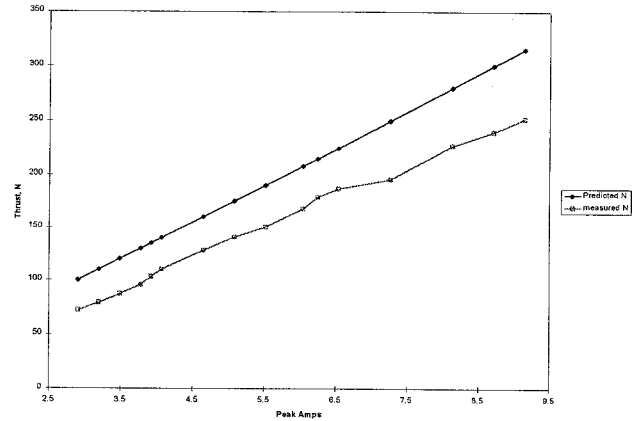


Fig. 5. Thrust Measurements

The actual axial thrust measurements are about 80% of the predicted value from the tubular motor analysis as seen in Fig. 5. We suspect the main cause of the offset in the graph is the friction in the guide rail for the platen. The friction range as measured with a spring gage is on the order of 20 N . Also, even if we use an air gap value that averages the spacing from the minimum air gap to the corners between the magnets, it does not account for the missing spaces between the magnets. Thus, our predicted thrust values are higher than physically realizable by the system. The 20% averaged error between the predicted and measured thrust values seems reasonable considering these error sources. This discrepancy bears further study.

B. Step Response

The response of the system to a 25.4-mm (1-in) step command is shown in Fig. 6. Note that the plot shows the response in units of inches. The system demonstrated typical rise times of 50 ms in response to step inputs. The motor exhibits problems with dynamic stiffness that we have not been able to debug in this preliminary study, as well as high overshoot and excess lag response.

The step responses of the system are repeatable up to steps of 5 cm (2 in), displaying overshoot of 15% for small steps and up to 40% for 5-cm steps. After steps of that size, the overshoot of the platen can reach 50% or above. For steps greater than 10 cm (4 in), the overshoot can cause the system to loose control of the platen. At present, the antiwindup of the controller limits both the lead integration command and the overall command to 600 N . This is close to twice the maximum output capability of the motor, and the current signals are limited to 10 A in code. The plateau seen after the initial overshoot peak is caused by this unoptimized antiwindup approach.

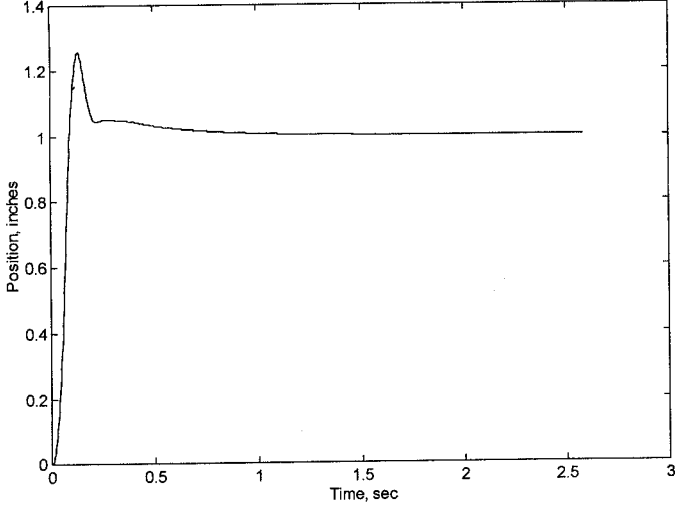


Fig. 6. Step Response

VI. CONCLUSIONS

The main purpose of this research is the analysis and design of a tubular linear permanent-magnet motor for a machine tool application. We derived transfer relations and numerical force estimations for a tubular linear permanent-magnet motor with a Halbach magnet array. Preliminary experimental thrust measurements are given to confirm the theoretical predictions. These predictions are matched within a reasonable error bound. The commutation laws are derived for the tubular motor via a Cartesian approximation.

The tubular motor is a moving-magnet-stationary-winding type, whose windings are wound around an aluminum coolant pipe. This offers the possibility of establishing efficient cooling for the stator windings. The temperature estimates based on our model show some discrepancy with predicted values. The main reason for the discrepancy is the lower thermal conductivity in the stator due to the insulation layer and air around the copper wires. These hinder the thermal flow radially inward to the aluminum pipe that contains the coolant.

We provide a preliminary step response. The system would typically settle to within 50 μm of the commanded position. The maximum velocity is limited to 1.0 m/s due to the linear encoder specification. While more work remains to address the limitations of the present design, this tubular motor topology holds promise for use in the machine tool applications.

APPENDIX

A. Field Solutions for Permanent-Magnet Tubular Motors

Let $\mathbf{A}_n = (\tilde{A}_{rn}\mathbf{i}_r + \tilde{A}_{\theta n}\mathbf{i}_\theta + \tilde{A}_{zn}\mathbf{i}_z)e^{-jk_n z}$. We define \mathbf{B}_n , \mathbf{M}_n and \mathbf{K}_n likewise. By the geometry of the tubular

motor, the vector potential has only θ -component. In cylindrical coordinates,

$$\begin{aligned}\mathbf{B}_n &\equiv \nabla \times \mathbf{A}_n \\ &= jk_n \tilde{A}_{\theta n} e^{-jk_n z} \mathbf{i}_r + \left(\frac{\tilde{A}_{\theta n}}{r} + \frac{d}{dr} \tilde{A}_{\theta n} \right) e^{-jk_n z} \mathbf{i}_z.\end{aligned}$$

So,

$$\tilde{B}_{rn} = jk_n \tilde{A}_{\theta n} \quad (28)$$

$$\tilde{B}_{zn} = \frac{\tilde{A}_{\theta n}}{r} + \frac{d}{dr} \tilde{A}_{\theta n}. \quad (29)$$

By setting the Coulomb gauge,

$$\begin{aligned}\nabla^2 \mathbf{A}_n &= -\nabla \times \nabla \times \mathbf{A}_n \\ &= \left(\frac{d^2 \tilde{A}_{\theta n}}{dr^2} + \frac{1}{r} \frac{d\tilde{A}_{\theta n}}{dr} - \left(k_n^2 + \frac{1}{r^2} \right) \tilde{A}_{\theta n} \right) e^{-jk_n z} \mathbf{i}_\theta.\end{aligned} \quad (30)$$

The homogeneous part of the Poisson equation has the form of modified Bessel equation [11].

1) *Fields due to Magnet*: The curl of the n th-order term of the magnetization in axisymmetric coordinates is calculated as

$$\nabla \times \mathbf{M}_n = -jk_n \frac{\tilde{M}_{rn}}{r'} e^{-jk_n z'} \mathbf{i}_{\theta'}. \quad (31)$$

The Ampere's law with magnetic material is $\nabla \times \mathbf{B} = \mu_0(\mathbf{J}_f + \nabla \times \mathbf{M})$. With absence of free current density \mathbf{J}_f in the magnet region, the Fourier coefficients $\tilde{A}_{\theta n}$ of the θ -component of the vector potential satisfy the following scalar Poisson equation.

$$\frac{d^2 \tilde{A}_{\theta n}}{dr'^2} + \frac{1}{r'} \frac{d\tilde{A}_{\theta n}}{dr'} - \left(k_n^2 + \frac{1}{r'^2} \right) \tilde{A}_{\theta n} = \mu_0 \frac{jk_n}{r'} \tilde{M}_{rn} \quad (32)$$

By inspection, a particular solution could be

$$\tilde{A}_{\theta np} = \begin{cases} -\frac{j\mu_0}{k_n r} \tilde{M}_{rn} & (n \neq 0) \\ \frac{j\mu_0 k_n}{2} r \ln r \tilde{M}_{rn} & (n = 0) \end{cases} \quad (33)$$

Since there is no DC magnetization, no zeroth-order vector potential exists. With the particular solution in (33), $\frac{1}{r'} \frac{d}{dr'} (r' \tilde{A}_{\theta np}) = 0$, so, $\tilde{B}_{zn} = \frac{1}{r'} \frac{d}{dr'} (r' \tilde{A}_{\theta n}) = \frac{1}{r'} \frac{d}{dr'} (r' \tilde{A}_{\theta nh})$, where $\tilde{A}_{\theta nh}$ are the homogeneous solutions. Then, the transfer relations for the magnet are [8]

$$\begin{bmatrix} \tilde{B}_{zn}^f \\ \tilde{B}_{zn}^g \end{bmatrix} = -k_n^2 \begin{bmatrix} F_0(\delta, \gamma) & G_0(\gamma, \delta) \\ G_0(\delta, \gamma) & F_0(\gamma, \delta) \end{bmatrix} \begin{bmatrix} \tilde{A}_{\theta n}^f - \tilde{A}_{\theta np}(\gamma) \\ \tilde{A}_{\theta n}^g - \tilde{A}_{\theta np}(\delta) \end{bmatrix}. \quad (34)$$

Using the particular solution (33) we chose,

$$\begin{bmatrix} \tilde{B}_{zn}^f \\ \tilde{B}_{zn}^g \end{bmatrix} = -k_n^2 \begin{bmatrix} F_0(\delta, \gamma) & G_0(\gamma, \delta) \\ G_0(\delta, \gamma) & F_0(\gamma, \delta) \end{bmatrix} \begin{bmatrix} \tilde{A}_{\theta n}^f \\ \tilde{A}_{\theta n}^g \end{bmatrix} - j\mu_0 k_n \tilde{M}_{rn} \begin{bmatrix} F_0(\delta, \gamma)/\gamma + G_0(\gamma, \delta)/\delta \\ G_0(\delta, \gamma)/\gamma + F_0(\gamma, \delta)/\delta \end{bmatrix}. \quad (35)$$

Equivalent surface current densities at the boundary (f) and (g) are

$$K_n^f = M_n \times \mathbf{i}_{r'} = \tilde{M}_{zn} e^{-jk_n z'} \mathbf{i}_{\theta'} \quad (36)$$

$$K_n^g = M_n \times (-\mathbf{i}_{r'}) = -\tilde{M}_{zn} e^{-jk_n z'} \mathbf{i}_{\theta'}. \quad (37)$$

So, the boundary conditions for magnetic flux density are

$$-\tilde{B}_{zn}^e + \tilde{B}_{zn}^f = \mu_0 \tilde{M}_{zn} \quad (38)$$

$$-\tilde{B}_{zn}^g + \tilde{B}_{zn}^h = -\mu_0 \tilde{M}_{zn}. \quad (39)$$

Solving (35) and (38–39) with the continuity of the vector potential, we obtain the axial components of flux density.

$$\begin{bmatrix} \tilde{B}_{zn}^e \\ \tilde{B}_{zn}^h \end{bmatrix} = \begin{bmatrix} 1 - \gamma_n \frac{K_1(\gamma_n \gamma)}{K_0(\gamma_n \gamma)} F_0(\delta, \gamma) & \gamma_n \frac{I_1(\gamma_n \delta)}{I_0(\gamma_n \delta)} G_0(\gamma, \delta) \\ -\gamma_n \frac{K_1(\gamma_n \gamma)}{K_0(\gamma_n \gamma)} G_0(\delta, \gamma) & 1 + \gamma_n \frac{I_1(\gamma_n \delta)}{I_0(\gamma_n \delta)} F_0(\gamma, \delta) \end{bmatrix}^{-1}$$

$$\cdot \begin{bmatrix} -\mu_0 \tilde{M}_{zn} - j\mu_0 k_n \tilde{M}_{rn} \{F_0(\delta, \gamma)/\gamma + G_0(\gamma, \delta)/\delta\} \\ -\mu_0 \tilde{M}_{zn} - j\mu_0 k_n \tilde{M}_{rn} \{G_0(\delta, \gamma)/\gamma + F_0(\gamma, \delta)/\delta\} \end{bmatrix} \quad (40)$$

By the transfer relations outside and inside the magnet region,

$$\begin{bmatrix} \tilde{A}_{\theta n}^e \\ \tilde{A}_{\theta n}^h \end{bmatrix} = \begin{bmatrix} -\frac{1}{\gamma_n} \frac{K_1(\gamma_n \gamma)}{K_0(\gamma_n \gamma)} \tilde{B}_{zn}^e \\ \frac{1}{\gamma_n} \frac{I_1(\gamma_n \delta)}{I_0(\gamma_n \delta)} \tilde{B}_{zn}^h \end{bmatrix}. \quad (41)$$

And by (28),

$$\begin{bmatrix} \tilde{B}_{rn}^e \\ \tilde{B}_{rn}^h \end{bmatrix} = \begin{bmatrix} jk_n \tilde{A}_{\theta n}^e \\ jk_n \tilde{A}_{\theta n}^h \end{bmatrix}. \quad (42)$$

Equations (40) and (42) specify the field on the surfaces of the magnetized region.

2) *Field due to Stator Current*: Let us consider the following simplified version of the Poisson equation. (Cf. (32)).

$$\frac{d^2 \tilde{A}_{\theta n}}{dr^2} + \frac{1}{r} \frac{d\tilde{A}_{\theta n}}{dr} - \left(k_n^2 + \frac{1}{r^2}\right) \tilde{A}_{\theta n} = -\mu_0 \frac{1}{r} \tilde{J}_{\theta n} \quad (43)$$

The zeroth-order term does not exist in the balanced operation. As in (33), a particular solution for $n \neq 0$ could be $\tilde{A}_{\theta np} = \frac{\mu_0}{k_n^2 r} \tilde{J}_{\theta n}$. Now the derivation of the transfer relations is technically the same as in the magnet array case. So, the transfer relations for the current distribution are

$$\begin{bmatrix} \tilde{B}_{zn}^a \\ \tilde{B}_{zn}^d \end{bmatrix} = -k_n^2 \begin{bmatrix} F_0(\beta, \alpha) & G_0(\alpha, \beta) \\ G_0(\beta, \alpha) & F_0(\alpha, \beta) \end{bmatrix} \begin{bmatrix} \tilde{A}_{\theta n}^a \\ \tilde{A}_{\theta n}^d \end{bmatrix} + \mu_0 \tilde{J}_{\theta n} \begin{bmatrix} F_0(\beta, \alpha)/\alpha + G_0(\alpha, \beta)/\beta \\ G_0(\beta, \alpha)/\alpha + F_0(\alpha, \beta)/\beta \end{bmatrix}. \quad (44)$$

There is no surface current density at the boundary (b) and (c). So, the tangential components of the magnetic flux density should be continuous.

$$-\tilde{B}_{zn}^a + \tilde{B}_{zn}^b = 0 \quad (45)$$

$$-\tilde{B}_{zn}^c + \tilde{B}_{zn}^d = 0 \quad (46)$$

Solving (44) and (45–46) with the continuity of the vector potential, we obtain the axial component of flux density.

$$\begin{bmatrix} \tilde{B}_{zn}^a \\ \tilde{B}_{zn}^d \end{bmatrix} = \begin{bmatrix} 1 - \gamma_n \frac{K_1(\gamma_n \alpha)}{K_0(\gamma_n \alpha)} F_0(\beta, \alpha) & \gamma_n \frac{I_1(\gamma_n \beta)}{I_0(\gamma_n \beta)} G_0(\alpha, \beta) \\ -\gamma_n \frac{K_1(\gamma_n \alpha)}{K_0(\gamma_n \alpha)} G_0(\beta, \alpha) & 1 + \gamma_n \frac{I_1(\gamma_n \beta)}{I_0(\gamma_n \beta)} F_0(\alpha, \beta) \end{bmatrix}^{-1} \cdot \mu_0 \tilde{J}_{\theta n} \begin{bmatrix} F_0(\beta, \alpha)/\alpha + G_0(\alpha, \beta)/\beta \\ G_0(\beta, \alpha)/\alpha + F_0(\alpha, \beta)/\beta \end{bmatrix} \quad (47)$$

By the transfer relations outside and inside the current region,

$$\begin{bmatrix} \tilde{A}_{\theta n}^a \\ \tilde{A}_{\theta n}^d \end{bmatrix} = \begin{bmatrix} -\frac{1}{\gamma_n} \frac{K_1(\gamma_n \alpha)}{K_0(\gamma_n \alpha)} \tilde{B}_{zn}^a \\ \frac{1}{\gamma_n} \frac{I_1(\gamma_n \beta)}{I_0(\gamma_n \beta)} \tilde{B}_{zn}^d \end{bmatrix}. \quad (48)$$

And

$$\begin{bmatrix} \tilde{B}_{rn}^a \\ \tilde{B}_{rn}^d \end{bmatrix} = \begin{bmatrix} jk_n \tilde{A}_{\theta n}^a \\ jk_n \tilde{A}_{\theta n}^d \end{bmatrix}. \quad (49)$$

Equations (47) and (49) specify the field on the surfaces of the stator current region.

REFERENCES

- [1] J. J. Cathey, D. A. Topmiller and S. A. Nasar, "A tubular self-synchronous motor for artificial heart pump drive," *IEEE Transactions on Biomedical Engineering*, vol. 33, no. 3, pp. 315–319, March 1986.
- [2] R. Akmes and J. F. Eastham, "Optimum design of brushless tubular linear machines," *IEEE Transactions on Magnetics*, vol. 26, no. 5, pp. 2547–2549, September 1990.
- [3] D. J. de Groot and C. J. Heuvelman, "Tubular linear induction motor for use as a servo Actuator," *IEE Proceedings*, vol. 137, Pt. B, No. 4, pp. 273–280, July 1990.
- [4] K. Halbach, "Design of permanent multipole magnets with oriented rare earth cobalt material," *Nuclear Instruments and Methods*, vol. 169, no. 1, pp. 1–10, 1980.
- [5] D. L. Trumper, W.-J. Kim and M. E. Williams, "Design and analysis framework for linear permanent-magnet machines," *IEEE Transactions on Industry Applications*, vol. 32, no. 2, pp. 371–379, March/April 1996.
- [6] J. Ofori-Tenkorang and J. H. Lang, "A comparative analysis of torque production in Halbach and conventional surface-mount permanent-magnet synchronous motors," in the *Proceedings of the IEEE IAS 30th Annual Meeting*, pp. 657–663, October 1995.
- [7] W.-J. Kim and D. L. Trumper, "Force ripple in surface-wound permanent-magnet linear motors," in the *Proceedings of the IEEE International Magnetics Conference*, April 1996.
- [8] J. R. Melcher, *Continuum Electromechanics*, MIT Press, 1981.
- [9] F. P. Incropera and D. P. DeWitt, *Fundamentals of Heat and Mass Transfer*, John Wiley & Sons, Inc., 1990.
- [10] G. F. Franklin, J. D. Powell and M. L. Workman, *Digital Control of Dynamic Systems*, 2nd Ed., Addison Wesley Publishing Co., Inc., 1990.
- [11] G. Arfken, *Mathematical Methods for Physicists*, 3rd Ed., Academic Press, 1985.